Correspondence_____

Pure Phase-Encoded MRI and Classification of Solids

Pratik Ghosh, David H. Laidlaw, Kurt W. Fleischer,
Alan H. Barr, and Russell E. Jacobs

Abstract—In this work, we combine a pure phase-encoded Magnetic Resonance Imaging (MRI) method with a new tissue-classification technique to make geometric models of a human tooth. We demonstrate the feasibility of three-dimensional imaging of solids using a conventional 11.7-T NMR spectrometer. In solid-state imaging, confounding line-broadening effects are typically eliminated using coherent averaging methods. Instead, we circumvent them by detecting the proton signal at a fixed phase-encode time following the radio-frequency excitation. By a judicious choice of the phase-encode time in the MR imaging protocol, we differentiate enamel and dentine sufficiently to successfully apply a new classification algorithm. This tissue-classification algorithm identifies the distribution of different material types, such as enamel and dentine, in volumetric data. In this algorithm, we treat a voxel as a volume, not as a single point, and assume that each voxel may contain more than one material. We use the distribution of MR image intensities within each voxel-sized volume to estimate the relative proportion of each material using a probabilistic approach. This combined approach, involving MRI and data classification, is directly applicable to bone imaging and hard-tissue contrast-based modeling of biological solids.

I. INTRODUCTION

In this paper, we apply a new tissue-discrimination algorithm to a three-dimensional (3-D) proton magnetic resonance image of a tooth that was obtained using an atypical solid-state imaging technique. Conventional MRI methods image the distribution of mobile water protons in specimens where the linewidths are on the order of a few Hertz. However, the proton linewidths in solids are on the order of kiloHertz. These large linewidths drastically limit the applicability of standard liquid-imaging techniques for three reasons: mapping the spatial information into the frequency-domain requires large magnetic-field gradients; digitizing signals from this wide frequency spread requires a proportionally wide receiver bandwidth; and the increased noise from this wider receiver bandwidth necessitates more signal averaging, thereby increasing total imaging time. As a result, solid-state imaging has relied almost exclusively on experimental line-narrowing approaches aimed at suppressing effects from homonuclear dipolar coupling, and from chemical and susceptibility shifts [1]–[3]. Recently, a novel approach that overcomes these line-broadening effects in MR images, first

introduced in one dimension in 1985 [4], has been successfully demonstrated using standard imaging accessories [5]; no hardware that is specific to solid-state spectroscopy or solid-state imaging was used. This so-called "constant time" imaging method uses pure phase encoding of all spatial information, unlike methods that use pure frequency encoding [6]–[8], or conventional Fourier Transform methods that use mixed phase and frequency encoding [9], [10]. In contrast to chemical shift imaging, which also involves phase encoding of the spatial dimensions [11], the effects from the chemical and susceptibility shifts are circumvented by encoding only one k-space point at a fixed phase-encode time following the radio-frequency (RF) excitation. Therefore, the presence of chemical shift or dipolar interactions causes signal loss, but does not introduce spatial distortions [5]. We use a "constant time" protocol to image protons in a human molar tooth, using a conventional 11.7-T NMR spectrometer (500 MHz for ^1H) equipped with microscopic imaging accessories.

We apply a new classification algorithm to the data collected from the human molar tooth. This classification process is the first step in creating geometric models of different materials. There has been much work done on material classification in sampled data [12], but many techniques introduce artifacts, particularly at the boundaries between different materials. These artifacts tend to appear as jaggy stair-steps or as anomalous additional surfaces in images and models derived from the classified data. Discrete statistical classification techniques are often used to map each sample in a dataset to a single material [13], [14]. These techniques work well in regions where only one material is present, as in the interiors of homogeneous regions, but they are less accurate near boundaries between these regions, where each sampled point represents multiple materials (see Fig. 1).

Methods that model each sample by representing it as a mixture of materials improve the classification results [15], [16]. These techniques classify each voxel based on a single measurement, effectively treating each voxel as a single point; instead, we reconstruct a continuous function from the data collected. Over each voxel-sized region, we create a histogram of this continuous function.

Our classification technique builds on a statistical framework. Given the histogram of a voxel-sized region, we use Bayesian probability theory and approximations of conditional and prior probabilities [17] to calculate the probability of a particular mixture of materials. We then find the most likely mixture for the region. We assume (as in Fig. 1) that each voxel is a mixture of materials, with mixtures like "A and B" occurring where partial-volume effects from the MRI sampling blur measurements of pure materials together. From this assumption, we derive basis functions that model histograms for pure materials and for mixtures of two materials. By using a reconstructed, continuous function derived from the data, and not just a single measurement, we incorporate more information into the classification process, thus increasing its accuracy. This additional information enables clear delineation of the air, enamel, and dentine boundaries in the tooth MR image.

II. METHODS

A. Imaging

In this section, we outline the MR imaging methods used. The *imaging experiments were carried out on a Bruker-AMX 500-MHz*
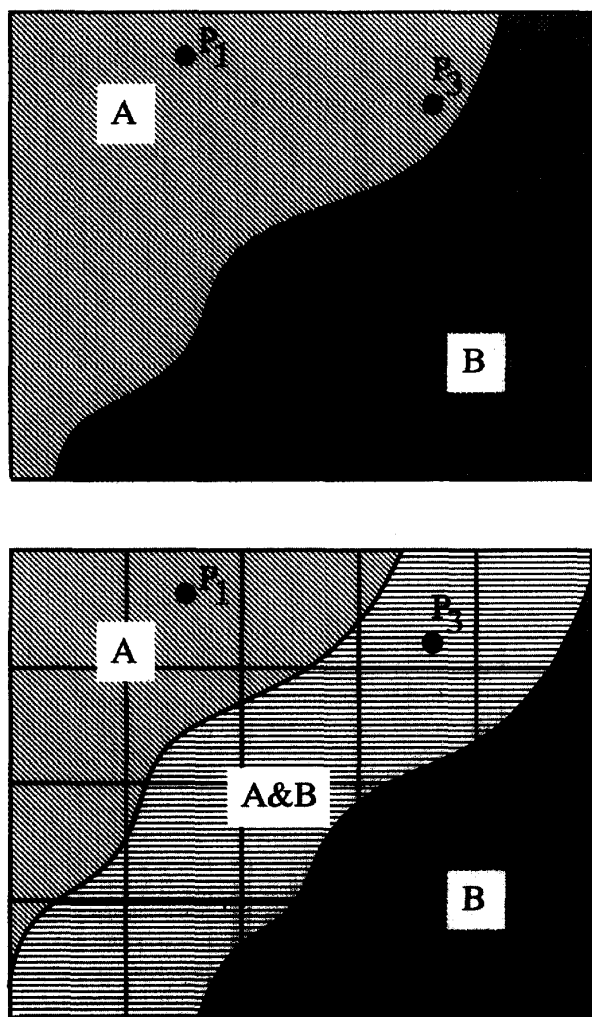
Fig. 1. Effects of sampling on material boundaries: (top) object, and (bottom) sampled data. We start from the assumption that in a real-world object each point is exactly one material, as in the top image. The measurement process removes high frequencies from the data and blurs sharp boundaries between materials. This process creates voxels that artificially contain mixtures of materials. Points P_1 and P_2 lie inside regions of a single material. Point P_3 lies near a boundary between materials; the bottom image contains the "A&B" region, where materials A and B are mixed.

89-mm vertical-bore system. A molar tooth was extracted from a 50-year old skull of a young woman, mounted at the end of a 10-mm glass tube, and positioned inside a 15-mm modified Alderman-Grant RF coil [18]. Because of the solid-state nature of teeth, some components of the spin-spin relaxation time constants, T_2, are less than 500 μs, resulting in an apparent time constant, T_2^*, at 500 MHz of 50–400 μs (see Section III). The gradient stabilization time for our air-cooled, unshielded, 43-mm ID gradient coil set is 300 μs. Because signal intensity rapidly decays within the switching-and-stabilization time, conventional imaging methods, which require that gradients be switched on/off within a single scan of the imaging sequence, are not feasible. To circumvent this problem, we used the pulse sequence shown in Fig. 2 [5]; it does not require any gradient switching within a scan. Magnetic field gradients (G) are switched on before the excitation and detection. They are incremented
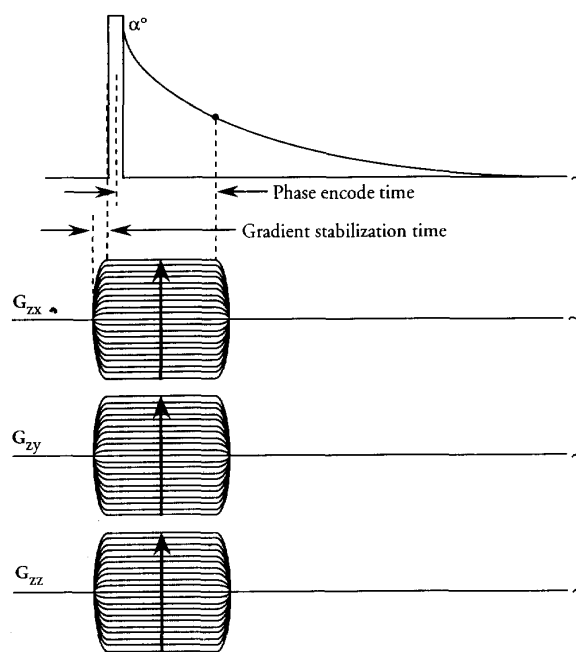

Fig. 2. Schematic diagram of the MRI pulse sequence used. The gradients are allowed to stabilize before the RF pulse is applied. After a fixed phase-encode time, the phase and amplitude of the magnetization are measured. The gradients are then turned off.

in equal steps along three orthogonal directions to scan k-space, where $k = \gamma G T_P / 2\pi$, T_P is the phase-encode time, and γ is the gyromagnetic ratio. T_P is set to provide contrast between the two components in the tooth (see Fig. 3), subject to the need to minimize total acquisition time and not overheat the gradient coils.

The nonselective RF-pulse duration must be small enough that the entire distribution of frequencies, including any introduced by the largest-applied magnetic field gradient, is irradiated. We use the maximum available transmitter power of 50 W, which limits the minimum achievable duration of the tip angle, α. The optimal signal-to-noise ratio for a given imaging time can be achieved if α; T_R, the pulse repetition time; and T_1, the spin-lattice relaxation time, satisfy $\cos \alpha = \exp(-T_R/T_1)$ [19]. If this relation is satisfied, α is the Ernst angle. Because we cannot satisfy this condition without either making the RF duration too long to irradiate the entire frequency spread or making T_R so short that we exceeded the maximum allowable duty cycle for our air-cooled gradient coil set, we use the maximum allowable tip angle that irradiates the required frequencies, and the minimum pulse-repetition time that does not overheat the gradient coils. If a water-cooled gradient coil system were used, a shorter T_R could be employed. This might allow use of the Ernst angle for irradiation, thus leading to a shorter overall imaging time with optimal signal intensity. We emphasize that a single point in k-space is acquired for each excitation; thus, the total time for data acquisition of an image is $N_k N_R T_R$, where N_k is the total number of encoded k-space points, and N_R is the number of averages.

B. Tissue Classification

In this section, we outline the classification problem, state our assumptions about the data we classify, and sketch the algorithm and its derivation. A detailed derivation and description of the implementation is given in [20]. The input to our process is a sampled dataset that measures distinguishing properties of the underlying
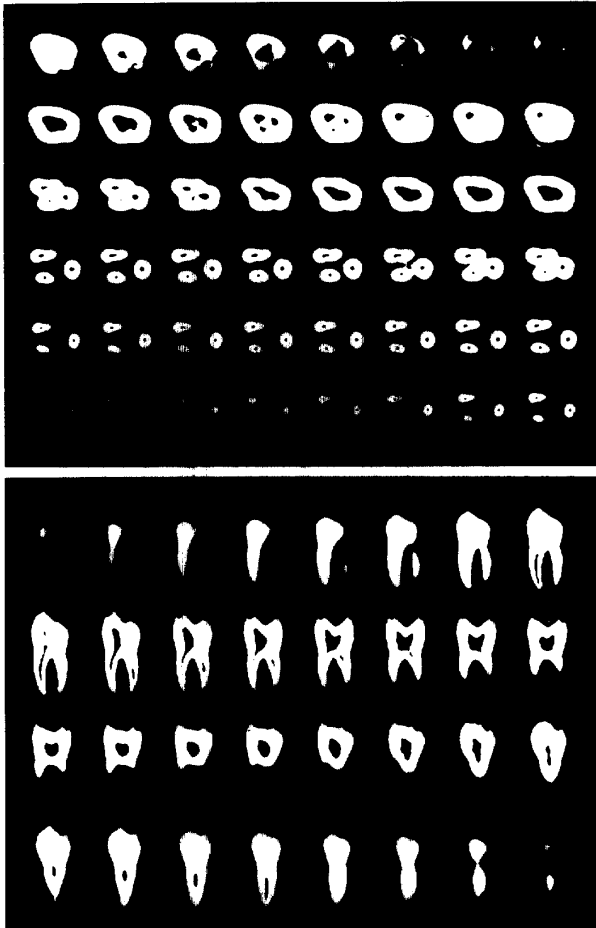
Fig. 3. Contiguous frames from a 3-D, ^{1}H image of a human tooth reconstructed with 128^3 isotropic voxels, 312 μm on a side. An RF pulse of 9°, 2.7 μs at 50 W was used to excite the tooth. A phase-encode time of 80 μs and a maximum gradient strength of 47 G cm^{-1} were used. Repetition time of 30 ms and two averages accounted for a total experiment time of 36 h. The top view shows frames perpendicular to the crown-apical axis. The top row shows the dentine-enamel structures, while the bottom row highlights the root structures. The bottom view shows frames that are perpendicular to the bucca-lingual axis, further highlighting the progression of inner hollow structures.

materials, such as the MR images shown in Fig. 3. We reconstruct a continuous, bandwidth-limited function from these samples. The final result of our classification process is a sampled volume dataset. Each sample estimates the relative volumes of materials in a small region.

1) Assumptions: We make three assumptions about the measurement process: 1) a given material produces the same value wherever it occurs in the specimen, discounting noise, 2) the sampling theorem is satisfied, thus we can reconstruct a continuous function with little or no aliasing, and 3) noise in the data is additive and normally distributed. For many types of medical imaging data, including MRI, these assumptions hold reasonably well, or can be satisfied sufficiently with preprocessing [14], [21]. While the noise assumption (3)) is not strictly true due to the magnitude nature of reconstructed MR data, it is sufficiently accurate to produce good results. We also make an assumption about the *objects* we measure. At the scale of the measurements, we assume the objects contain no mixtures: each spatial location in the object is exactly one pure material.
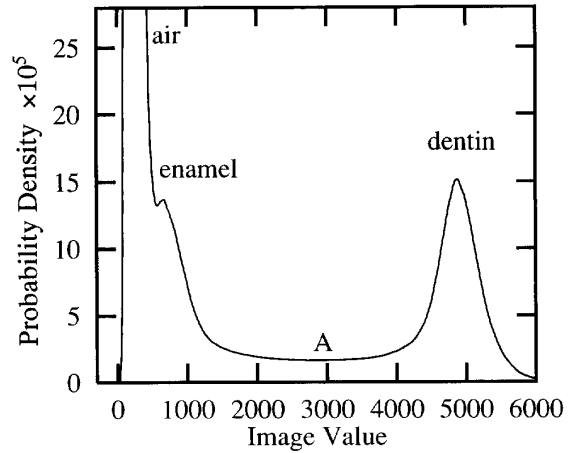

Fig. 4. Histogram of tooth dataset. The three peaks in the histogram correspond to air, enamel, and dentine. The values near these peaks represent voxels that are pure materials; the values between the peaks (e.g., at A in the graph) represent voxels that contain a mixture of materials.

2) Partial-volume "mixtures" introduced by the measurement process: Our assumption that each spatial location in the object is exactly one material does not imply that the same is true for the *measured* data, because of the data-collection and sampling process (see Fig. 1). The data are bandwidth limited to the Nyquist frequency by the measurement process. This filtering, or partial volume averaging, causes measurements of mixtures of materials to appear in areas where sharp boundaries between pure materials occur in the actual object. These "mixtures" cause problems for many classification algorithms because their signatures may coincide with the signatures of other materials. The algorithm presented here reduces boundary artifacts introduced by this ambiguity with a new approach that explicitly models "mixtures," and treats each voxel as a volume instead of a point sample.

3) The algorithm: This section gives a summary of the classification algorithm; details and more substantial derivations can be found in [20]. After we low-pass filter the MR data to remove aliasing, we calculate a histogram of the entire image, as shown in Fig. 4. We fit basis functions to this histogram. These inferred basis functions represent pure materials and their mixtures, and constitute a model of the materials that exist in the dataset.

Now that we have some idea of the materials present in the dataset, we can identify combinations of those materials in each voxel-sized region. We compute histograms over each of these regions. We then fit each histogram with a linear combination of the inferred material basis functions discovered from the analysis of the histogram over the entire dataset. These fits provide an estimate of the relative volume of each material in each voxel-sized region. Finally, we find isosurfaces [22] in the density images for each material, and use these to represent the surfaces between materials (see Fig. 5). The isosurface calculation and rendering are accomplished using the Application Visualization System [23].

4) The form of the basis functions: Each basis function represents a region containing either a single material or a mixture of two materials. The mixtures are assumed to have been created by partial volume averaging during the data collection process. The basis function that represents single materials is a normal distribution; for mixtures, the distribution is the convolution of a normal distribution and a box function that is nonzero between the mean signatures of
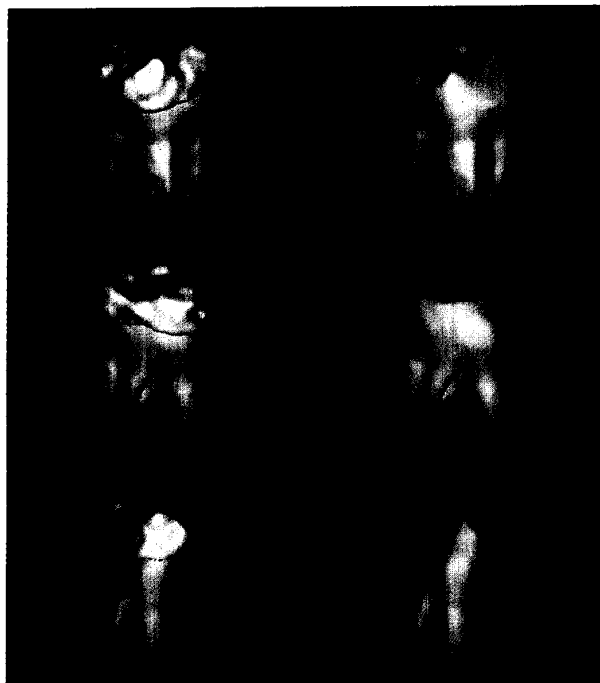
Fig. 5. Three pairs of corresponding views from a polygonal model of the tooth that was created by classifying enamel, dentine, and air from the reconstructed data in Fig. 3; and then automatically finding surfaces between the materials. The classification process identifies mixtures of materials within voxel-sized regions, allowing a more accurate surface model than techniques that assign a single material to each voxel. Both dentine and enamel are shown in the left images; the enamel has been removed in the right images, thus showing the shape of the dentine-enamel interface.

the materials comprising the mixture. The box function integrates to one. The form of the basis functions is derived from an equation for a continuous histogram and our assumptions about the measurement process and the objects we are measuring.

III. RESULTS

We show two views consisting of contiguous frames from a representative MR image of the tooth (18 mm $\times$ 12 mm) in Fig. 3. The roots and air-dentine-enamel interfaces are easily distinguished. The air-filled hollow structures inside the tooth show no signal. The dentine appears brightest, while the enamel appears as a dark gray halo around the top of the dentine structures. Fig. 5 shows the results of the classification, with surfaces rendered to indicate the enamel in white and the dentine in off-white. Computational removal of the enamel crown allows direct examination of the morphology of the dentine cap; it is here that the structure of the crown is initially determined as tooth development progresses [24].

In order to make a suitable choice of T_P, we measured T_2^* and T_2, using a small portion of another molar that was bored out to fit inside a 2-mm tube. A 4-mm solenoid RF coil was used so that the smallest possible pulse widths ($\pi_{pulse} \le 17$ μs) could be employed. The Fourier-transformed spectra of the time-domain NMR signals, from both the free-induction decay and the spin-echo, provided two peaks of different widths having T_2^* values of roughly 100 μs and 400 μs. The corresponding T_2 values were measured to be approximately 150 μs and 2 ms, using the Carr–Purcell–Meiboom–Gill (CPMG)

method [25]. We digitized the peak and the latter half of the spin echo so that very short echo times could be used. We measured the peak intensity from individual spin echoes acquired at different echo times, always waiting 15 s between experiments so that T_1 processes had disappeared. We thus avoided spin-lock type effects, and eliminated any π_{pulse}-width error effects on odd-echo intensities [26]. We fitted 40 time-domain spin-echo intensities to a bi-exponential function using the Levenberg–Marquardt nonlinear least-squares algorithm [27]. Based on the T_2^* values, a range of T_P of 50–200 μs was considered; where $T_P = T_2^*/2$ for maximum sensitivity [5]. A longer T_P sacrificed sensitivity for greater resolution, while a shorter T_P required a shorter RF duration. We chose a compromise value of $T_P = 80$ μs.

IV. CONCLUSION

We have successfully combined a novel MRI application with a new classification algorithm to produce a geometric model of a human tooth. We have demonstrated the feasibility of imaging biological solids with a pure phase-encoded MRI method. Using a judicious choice of phase-encode time, we have also achieved good contrast between different hard tissues. Although detection of only one complex data-point for every phase-encoding step makes total acquisition periods long, the resultant images are free from the effects of chemical and susceptibility shifts, as well as from dipolar broadening. This MRI implementation exemplifies a simple experimental set-up that can be employed for imaging biological solids [28]–[30], and is especially suitable for studying objects with very short spin-spin relaxation time constants; thus it is applicable to other nuclei as well. In vitro investigations of bone-mineral composition, as well as of endogenous fluoride, can be made by detecting the ^{31}P and ^{19}F MR signals [29], [31].

Our new algorithm for classifying volume data avoids artifacts at material boundaries by taking into account the mixtures introduced by the sampling and filtering processes. This is important for examining certain types of structures, such as the shape of the dentine-enamel interface shown in Fig. 5. Tooth morphology has been employed extensively in discussions of phylogeny and taxonomy [32], [33]. As the approach described herein highlights hard-tissue contrast and accurately models boundaries between materials, it will be directly applicable to morphometric and developmental studies of tooth and bone.

REFERENCES

[1] D. Cory, "Solid state NMR imaging," Annu. Rep. NMR Spectroscopy, vol. 24, pp. 87–180, 1992.
[2] P. Mansfield, P. Grannell, A. Garroway, and D. Stalker, "Multi-pulse line narrowing experiments: NMR 'diffraction' in solids?" in Pulsed Nuclear Magnetic Resonance and Spin Dynamics in Solids, J. Hennell, Ed. Krakow, Poland: Institute of Nuclear Physics, First Specialized "Colloque Ampere," 1973, pp. 16–27.
[3] P. Mansfield and P. Grannell, "Solid state NMR imaging," Phys. Rev. B, vol. 12, pp. 3618–3634, 1975.
[4] S. Emid and J. Creyghton, "High resolution NMR imaging in solids," Physica B, vol. 128, pp. 81–83, 1985.

[5] S. Gravina and D. Cory, "Sensitivity and resolution of constant-time imaging," *J. Magn. Reson., Ser. B*, vol. 104, pp. 53–61, 1994.

[6] P. Lauterbur, "Image formation by induced local interactions: Examples employing nuclear magnetic resonance," *Nature*, vol. 242, pp. 190–191, 1973.

[7] R. Marr, C.-N. Chen, and P. Lauterbur, "On two approaches to 3-D reconstruction in NMR zeugmatography," in *Mathematical Aspects of Computerized Tomography*, G. Herman and F. Natterer, Eds. New York: Springer-Verlag, 1981, vol. 8, pp. 225–240.

[8] X. Zhou and P. Lauterbur, "NMR microscopy using projection reconstruction," in *Magnetic Resonance Microscopy: Methods and Applications in Materials Science, Agriculture, and Biomedicine*, B. Blumich and W. Kuhn, Eds. New York: VCH, 1992, pp. 3–27.

[9] P. Morris, *Nuclear Magnetic Resonance in Medicine and Biology*. Oxford: Clarendon, 1986.

[10] P. Callaghan, *Principles of Nuclear Magnetic Resonance Microscopy*. Oxford: Clarendon, 1993.

[11] T. Brown, B. Kincaid, and K. Ugurbil, "NMR chemical shift imaging in three dimensions," in *Proc. Nat. Acad. Sci., USA*, vol. 79, pp. 3523–3526, 1982.

[12] R. Duda and P. Hart, *Pattern Classification and Scene Analysis*. New York: Wiley, 1973.

[13] M. Vannier, R. Butterfield, D. Jordan, W. Murphy, R. Levitt, and M. Gado, "Multispectral analysis of magnetic resonance images," *Radiol.*, vol. 154, pp. 221–224, 1985.

[14] M. Vannier, C. Speidel, and D. Rickman, "Magnetic resonance imaging multispectral tissue classification," *News Physiol. Sci.*, vol. 3, pp. 148–154, Aug. 1988.

[15] R. Drebin, L. Carpenter, and P. Hanrahan, "Volume rendering," in *Comput. Graphics (SIGGRAPH '88 Proceedings)*, J. Dill, Ed., vol. 22, pp. 65–74, Aug. 1988.

[16] H. Choi, D. Haynor, and Y. Kim, "Partial volume tissue classification of multichannel magnetic resonance images—A mixel model," *IEEE Trans. Med. Imag.*, vol. 10, pp. 395–407, 1991.

[17] T. Loredo, "From Laplace to supernova SN1987A: Bayesian inference in astrophysics," in *Maximum Entropy and Bayesian Methods*, P. Fougere, Ed. Denmark: Kluwer, 1989.

[18] D. Alderman and D. Grant, "An efficient decoupler coil design which reduces heating in conductive samples in superconducting spectrometers," *J. Magn. Reson.*, vol. 36, pp. 447–451, 1979.

[19] R. Ernst and W. Anderson, "Application of Fourier transform spectroscopy to magnetic resonance," *Rev. Sci. Instrum.*, vol. 37, pp. 93–102, 1966.

[20] D. Laidlaw, K. Fleischer, and A. Barr, "Classification of material mixtures in volume data for visualization and modeling," California Inst. of Technol., Pasadena, CA, Tech. Rep. CS-TR-94-07, 1994.

[21] D. Laidlaw, "Material classification of magnetic resonance volume data," M.S. thesis, California Inst. of Technol., Pasadena, CA, Tech. Rep. CS-TR-92-21, 1992.

[22] W. Lorensen and H. Cline, "Marching cubes: A high resolution 3-D surface construction algorithm," in *Comput. Graphics (SIGGRAPH '87 Proceedings)*, M. Stone, Ed., vol. 21, pp. 163–169, July 1987.

[23] C. Upson, T. Faulhaber, Jr., D. Kamins, D. Laidlaw, D. Schlegel, J. Vroom, R. Gurwitz, and A. van Dam, "The application visualization system: A computational environment for scientific visualization," *IEEE Comput. Graphics Applicat.*, vol. 9, no. 4, pp. 30–42, 1989.

[24] W. Gaunt and A. Miles, "Fundamental aspects of tooth morphogenesis," in *Structural and Chemical Organization of Teeth*, A. Miles, Ed. New York: Academic, 1967, vol. 1, pp. 151–197.

[25] S. Meiboom and D. Gill, "Modified spin-echo method for measuring nuclear relaxation times," *Rev. Sci. Instrum.*, vol. 29, pp. 688–691, 1958.

[26] B. Gerstein and C. Dybowski, *Transient Techniques in NMR of Solids: An Introduction to Theory and Practice*. Orlando: Academic, 1985.

[27] W. Press, S. Teukolsky, W. Vetterling, and B. Flannery, *Numerical Recipes in C: The Art of Scientific Computing*, 2nd ed. New York: Cambridge Univ. Press, 1992, pp. 683–688.

[28] J. Ackerman, L. Garrido, J. Moore, B. Pfleiderer, and Y. Wu, "Fluid and solid state MRI of biological and nonbiological ceramics," in *Magnetic Resonance Microscopy: Methods and Applications in Materials Science, Agriculture, and Biomedicine*, B. Blumich and W. Kuhn, Eds. New York: VCH, 1992, pp. 237–260.

[29] J. Ackerman, D. Raleigh, and M. Glimcher, "P-31 magnetic resonance imaging of hydroxyapatite—A model for bone imaging," *Magn. Reson. Med.*, vol. 25, pp. 1–11, 1992.

[30] Z. Wu, H. Chung, and F. Wehrli, "A Bayesian approach to subvoxel tissue classification in NMR microscopic images of trabecular bone," *Magn. Reson. Med.*, vol. 31, pp. 302–308, 1994.

[31] R. Code, J. Harrison, K. McNeill, and M. Szyjkowski, "*In vivo* F-19 spin relaxation in index finger bones," *Magn. Reson. Med.*, vol. 13, pp. 358–369, 1990.

[32] R. Martin, *Primate Origins and Evolution*. London: Chapman and Hall, 1991.

[33] P. Butler, E. Nevo, A. Beiles, and S. Simson, "Variations of molar morphology in the spalax ehrenbergi superspecies: Adaptive and phylogenetic significance," *J. Zool., London*, vol. 229, pp. 191–216, 1993.